This is a preprint, the final version is subject to change, of the American Mineralogist (MSA)
Cite as Authors (Year) Title. American Mineralogist, in press.
DOI: https://doi.org/10.2138/am-2019-6597

Revision 1

Crystallization of spherical (Mg,Fe)-oxides by particle attachment in the shocked Martian meteorite Northwest Africa 7755

Ai-Cheng Zhang[1,*], Shu-Zhou Wang[1], Naotaka Tomioka[2], Xian-Cai Lu[1], Zhi-Yuan Ding[3,4], Chi Ma[5], Peng Wang[3,4], Jia-Ni Chen[1], Sheng Xu[3,4], Li-Xin Gu[6], Yuan-Qiang Bai[7], Yang Li[8], Naoya Sakamoto[9], and Ru-Cheng Wang[1]

[1] State Key Laboratory for Mineral Deposits Research and School of Earth Sciences and Engineering, Nanjing University, Nanjing 210046, China

[2] Kochi Institute for Core Sample Research, Japan Agency for Marine-Earth Science and Technology (JAMSTEC), Nankoku, Kochi 783-8502, Japan

[3] National Laboratory of Solid State Microstructures, Nanjing University, Nanjing 210093, China

[4] College of Engineering and Applied Sciences and Collaborative Innovation Center of Advanced Microstructures, Nanjing University, Nanjing 210093, China

[5] Division of Geological and Planetary Sciences, California Institute of Technology, California 91125, USA

[6] Institute of Geology and Geophysics, Chinese Academy of Sciences, Beijing 100029, China

[7] Thermos Fisher Scientific, 1 Jalan Kilang Timor, #04-02 Pacific Tech Centre, Singapore 159303, Singapore

[8] Institute of Geochemistry, Chinese Academy of Sciences, Guiyang 550081, China

[9] Isotope Imaging Laboratory, Creative Research Institution, Hokkaido University, Sapporo 001-0021, Japan

*Corresponding author. E-mail address: aczhang@nju.edu.cn

For submission to ***American Mineralogist***

This is a preprint, the final version is subject to change, of the American Mineralogist (MSA)
Cite as Authors (Year) Title. American Mineralogist, in press.
DOI: https://doi.org/10.2138/am-2019-6597

ABSTRACT

Crystallization is one of the most fundamental processes for both solid inorganic and organic materials in nature. Classical crystallization model mainly involves monomer-by-monomer addition of simple chemical species. Recently, nanoparticle attachment has been realized as an important mechanism of crystallization in comparatively low-temperature aqueous natural and synthetic systems. However, no evidence of crystallization by particle attachment has been reported in petrologically important melts. In this study, we described spherical (Mg,Fe)-oxides with a protrusion surface in a shock-induced melt pocket from the Martian meteorite Northwest Africa 7755. Transmission electron microscopic observations demonstrate that the (Mg,Fe)-oxides are structure-coherent intergrowth of ferropericlase and magnesioferrite. The magnesioferrite is mainly present adjacent to the interface between (Mg,Fe)-oxides spherules and surrounding silicate glass, but not in direct contact with the silicate glass. Thermodynamic and kinetic considerations suggest that development of the spherical (Mg,Fe)-oxides can be best interpreted with crystallization by particle attachment and subsequent Ostwald Ripening. This indicates that crystallization by particle attachment can also take place in high-temperature melts and has potential implications for understanding the nucleation and growth of early-stage crystals in high-temperature melts, such as chondrules in the solar nebula, erupted volcanic melts, and probably even intrusive magmas.

Keywords: Crystallization by particle attachment; Ferropericlase; Magnesioferrite; Shock-induced melt pocket; Martian meteorite; Northwest Africa 7755

This is a preprint, the final version is subject to change, of the American Mineralogist (MSA)
Cite as Authors (Year) Title. American Mineralogist, in press.
DOI: https://doi.org/10.2138/am-2019-6597

INTRODUCTION

Nucleation and growth of crystals are fundamental processes during formation of natural and synthetic solid materials. Their mechanisms have been of long-term interest to scientists in the fields of physics, chemistry, material science, and earth and planetary sciences. Understanding the nucleation and growth mechanisms of crystals are not only important to interpret the formation and evolution of the organic and inorganic matters in nature, but also critical to control the physicochemical properties of synthetic materials.

Nucleation and growth models that involve monomer-by-monomer addition of simple chemical species can account for development of crystals in most natural and synthetic systems. However, in the past two decades, crystallization models involving particle attachment have been proposed to interpret abundant phenomena that were difficult to be interpreted with the monomer-by-monomer nucleation and growth models (e.g., Penn and Banfield 1998; Banfield et al. 2000). Recently, the evidence, indicators, consequences, pathways, and thermodynamic and kinetic considerations during crystallization by particle attachment, have been reviewed (Ivanov et al. 2014; De Yoreo et al. 2015). The crystallization by particle attachment usually involves an intermediate phase, which could be nanocrystal, poorly crystalline nanoparticle, amorphous nanoparticle, droplet, complex, and oligomer (De Yoreo et al. 2015). However, most of the systems involving crystallization by particle attachment are comparatively low-temperature systems, covering synthetic solution systems with organic matters, biogenic systems, and hydrothermal systems (De Yoreo et al. 2015). Recently, a two-step crystallization, which might be related to crystallization by particle attachment, has been proposed for the formation of Al_2O_3 particles in supersaturated vapor (e.g., Ishizuka et al. 2016).

Crystallization in high-temperature melts, typically petrologically important silicate melts, is one of the most ubiquitous and fundamental processes in our solar system, from the formation of earliest solids in the solar nebula 4.56 billion years ago, to the consolidation of magma oceans at the early stages of differentiated planets and asteroids, and to the present-day eruptions of volcanos on Earth. However, whether crystallization by particle attachment could occur in the early-stage growth of crystals in melts remains unconstrained up to date due to the following limitations. First, since crystallization by particle attachment could be only prevalent at the early stages of crystallization (De Yoreo et al. 2015), minerals in natural rocks might have experienced complex recrystallization and metamorphism, in which early-stage records probably have been obliterated. Second, it is very challenging to perform live observations on the nucleation and growth at a scale of nanoscale in silicate melts with in situ instruments (e.g., transmission electron microscope) at laboratory conditions.

Celestial collision is a dynamic process that has prevalently taken place in the solar system. It can cause localized high-temperature and high-pressure melting and rapid crystallization in rocks at a timescale down to seconds to microseconds (Sharp and DeCarli 2006). It is very likely that early-stage development of crystals by particle attachment from high-temperature melts has been recorded in shock melt veins or pockets, the products of celestial collision events. During studying mineralogy of shock-induced melt veins and pockets in meteorites (Pang et al. 2016, 2018; Wang et al. 2017), we observed the presence of spherical (Mg,Fe)-oxides with a protrusion surface in a shock-induced melt pocket from the Martian meteorite Northwest Africa (NWA) 7755. Here we report the textural, chemical, and structural features of these spherical (Mg,Fe)-oxides, based on detailed

observations with analytical transmission electron microscopy (ATEM). We argue that these spherical (Mg,Fe)-oxides could be products of crystallization by particle attachment in high-temperature melts.

ANALYTICAL METHODS

Petrographic textures of the lherzolitic shergottite NWA 7755 were studied using JEOL JSM-7000F field-emission scanning electron microscope (FE-SEM) with Backscattered electron (BSE) mode at Hokkaido University, Japan. An accelerating voltage of 15 kV with a beam current of 2–10 nA was used for making BSE images. Chemical compositions of ringwoodite were determined using a JEOL JXA-8100 electron probe micro-analyzer (EPMA) at Nanjing University, China. A focused beam of 20 nA at an accelerating voltage of 15 kV was used. A few natural and synthetic materials were used as standards. All EPMA data were reduced with the ZAF (atomic number-absorption-fluorescence) correction procedure.

In this study, four TEM foils were prepared with focused ion beam (FIB) technique. Three TEM foils were prepared at the Institute of Geology and Geophysics, Chinese Academy of Sciences, Beijing, China. The instrument is Zeiss Auriga Compact SEM-FIB instrument. One TEM foil was prepared at the Institute of Geochemistry, Chinese Academy of Sciences, Guiyang, China. The instrument is FEI Scios field emission scanning electron microscope. For both instruments, we deposited a layer of Pt over the region of interest to protect the surface from ion beam damage during sample preparation. After cutting, the foils were mounted on Cu grids using a micromanipulator and thinned to approximately 100 nm in thickness by a Ga-ion beam at an accelerating voltage of 30 kV with various

beam currents. The final polishing was performed at an accelerating voltage down to 2−4 kV.

The ultrathin foils were studied mainly using two FEI Tecnai F20 field emission transmission electron microscopes at Nanjing University. Both of the TEM instruments were operated at an accelerating voltage of 200 kV. The textures and morphology of minerals were observed with conventional TEM, and High-Angle Annular Dark Field scanning transmission electron microscopy (HAADF-STEM) modes. The crystallographic correlation between different phases were observed with high-resolution TEM (HRTEM) mode. The symmetry of minerals was determined using selected area electron diffraction (SAED). Dark-field images of (Mg,Fe)-oxides were taken to confirm the coexistence of multiple phases.

Chemical compositions of (Mg,Fe)-oxides and surrounding silicate glass were obtained with energy-dispersive X-ray spectroscopy (EDS) under STEM mode. The EDS detector was operated using AZtec software and FEI TEM User Interface control software. During the EDS analyses, the TEM sample stage was tilted for 15° toward the EDS detector. A ringwoodite aggregate, which composition was determined with EPMA technique, was used as an external standard to calibrate the k-factors for Mg, Fe, and Si. Theoretical k-factors of preinstalled experimental k-factors of the instruments were used for other elements (P, Ti, Al, Mn, and Ca). Chemical mapping was also performed in STEM mode to the distribution of Mg and Fe in different phases and to identify different minor phases (Fe-sulfide and Fe-phosphide).

The Fe $L_{2,3}$ electron energy loss spectra (EELS) of (Mg,Fe)-oxides, ringwoodite, and silicate glass were obtained using a FEI Titan Cubed G2 60-300 aberration corrected TEM

instrument at Nanjing University with mapping mode. The instrument was operated at an accelerating voltage of 300 kV using the dual-channel STEM-EELS acquisition for near-simultaneous low-loss and core-loss acquisition. The final EELS spectra for (Mg,Fe)-oxides, ringwoodite, and silicate glass were produced by integrating the spectra from selected areas to ensure the signal-to-noise ratio.

RESULTS

The meteorite NWA 7755 is a lherzolitic shergottite and consists mainly of olivine, pyroxene, plagioclase, chromite, ilmenite, and Ca-phosphate minerals. Its petrography and mineralogy have been reported in Wang et al. (2017). Due to strong shock metamorphism, both shock-induced melt veins and shock-induced melt pockets are present in NWA 7755. Olivine grains within and directly adjacent to shock-induced melt veins and shock-induced melt pockets have transformed into ringwoodite and $(Mg,Fe)_2SiO_4$ glass or have decomposed into ferropericlase and vitrified bridgmanite (Wang et al. 2017). Shock-induced melt veins in NWA 7755 consist of predominant bridgmanite with minor (Mg,Fe)-oxides, Fe-sulfide, Fe-phosphide, and Ca-phosphate minerals (Wang et al. 2017). The (Mg,Fe)-oxides associated with dissociation of olivine/ringwoodite mainly occur as spherical grains within silicate glass; however, those in shock-induced melt veins usually occur as an interstitial phase with an anhedral shape (Fig. 6b of Wang et al. 2017). In a shock-induced melt pocket of ~100 μm in its largest dimension, (Mg,Fe)-oxides commonly occur as spherules within silicate glass, especially adjacent to the surrounding ringwoodite (Fig. 1a). Some of them tend to form aggregates of oval-shaped grains (Fig. 1b). In some regions of the shock-induced melt pocket, a sandwich-like texture is observed that a

(Mg,Fe)-oxides-rich zone is located at the middle of two (Mg,Fe)-oxides-free zones (Fig. 1b).

All of the four FIB foils consist mainly of (Mg,Fe)-oxides (60 to 600 nm in diameter) and silicate glass. All the (Mg,Fe)-oxides grains have a protrusion surface (Fig. 2). Based on the HAADF-STEM images (e.g., Fig. 2), the protrusion usually varies at a scale of 10–20 nm. Fine-grained sulfide and phosphide (20–80 nm in size) are observed in the FIB foils and some of them occur as inclusions in spherules of (Mg,Fe)-oxides. Two grains of ringwoodite are present in one of the FIB foils (Fig. 3a). The composition of (Mg,Fe)-oxides that was determined by STEM-EDS has a small variation, with the Mg# value [Mg#=Mg/(Mg+Fe) in mole] varying from 0.58 to 0.67 (Table 1). The silicate glass surrounding the (Mg,Fe)-oxides contains major SiO_2, MgO, FeO, and minor CaO, Al_2O_3, and P_2O_5 (Table 2). The (Mg+Fe+Ca)/Si value in mole varies from 1.25 to 1.32, which is largely deviated from that for stoichiometric bridgmanite [(Mg+Fe+Ca)/Si=1]. The Mg# value (0.60–0.67) of the silicate glass is comparable to that of (Mg,Fe)-oxides.

Structures of the major phases in the FIB foils were determined with selected area electron diffraction (SAED). The silicate glass always has a diffuse diffraction pattern, indicating a glassy state. All of the spherical and oval-shaped (Mg,Fe)-oxides grains show well-defined SAED patterns and contain two sets of patterns with different reflection intensities (Fig. 4d). The stronger reflections can be indexed with a B1 structure of ferropericlase [(Mg,Fe)O], whereas the weaker reflections has spacing values just doubling those of ferropericlase and can be indexed only with a spinel structure. The two sets of SAED patterns always display a superposition relationship (e.g., Fp[001]//Mf[001], Fig. 4). Therefore, the SAED patterns (Fig. 4d) are derived from both ferropericlase and a phase

with a spinel structure from each (Mg,Fe)-oxides grain with structural coherency, which is consistent with the dark-field observation of the (Mg,Fe)-oxides grains (Fig. 5).

To further confirm that the observed spherical and oval-shaped (Mg,Fe)-oxides grains are a intergrowth of ferropericlase and a phase with a spinel structure, we performed STEM-EDS mapping and high-resolution TEM observations. In the HAADF-STEM image, a few spherical (Mg,Fe)-oxides grains have a thin and bright rim (Figs. 3b and 6a). The STEM-EDS mapping results reveal that the bright rim contains higher Fe and lower Mg than the interior (Fig. 6). High-resolution TEM observations reveal that the high-Fe and low-Mg phase has a spinel structure. This indicates that the phase with a spinel structure could be magnesioferrite (Fig. 7). The magnesioferrite occurs mainly adjacent to the boundary between silicate glass and the host ferropericlase and is structurally coherent to ferropericlase (Fig. 7). Meanwhile, it is noteworthy that magnesioferrite is not in direct contact with silicate glass. Instead, there is a thin layer (<5 nm) of ferropericlase between magnesioferrite and silicate glass (Fig. 7). In addition, the host ferropericlase region shows mottled contrasts with each domain of 2−10 nm in size (Fig. 7), which could be due to local strain contrast from different domains (Langenhorst et al. 2011; Hu and Sharp 2017).

The EELS results for the (Mg,Fe)-oxides, silicate glass, and ringwoodite were obtained to constrain the iron valence states (Fig. 8). The $Fe^{3+}/\Sigma Fe$ value calculated based on the universal technique by Van Aken and Liebscher (2002) is 0.33–0.42 for two different analyses on silicate glass. However, ferropericlase and relict ringwoodite have an $Fe^{3+}/\Sigma Fe$ value of 0.14 and 0.11, respectively.

DISCUSSION

Spherules of (Mg,Fe)-oxide in silicate glasses that are similar to those in this study in both spherical shape and SAED pattern have been reported in the shocked Tissint Martian meteorite (Fig. 5 of Hallis et al. 2017). Its SAED pattern was interpreted as a superlattice of ferropericlase (Hallis et al. 2017). In this study, however, the SAED patterns, dark-field image, and HRTEM observations indicate that the (Mg,Fe)-oxides spherules in NWA 7755 are an intergrowth of ferropericlase and magnesioferrite with structural coherency.

One of the striking features of (Mg,Fe)-oxides in this study is its spherical shape and the protrusion surface. The spherical shape imposes a possibility that the (Mg,Fe)-oxides within silicate glass could be a product of immiscible melts. However, this possibility can be excluded based on the following facts. First, ferropericlase that crystallized from high-pressure and high-temperature silicate melts has been observed in both natural and synthetic samples (e.g., Miyahara et al. 2011; Piet et al. 2016; Hu and Sharp 2017; Wang et al. 2017), with grain sizes similar to those in this study. If (Mg,Fe)-oxide melt, that is immiscible from a silicate melt under high-pressure and high-temperature conditions, was originally present, all of the ferropericlase grains would have a rounded shape due to the influence of surface energy and Kelvin effects. However, although the silicate glasses in these samples have a relatively large variation in chemical composition, the ferropericlase grains do not exhibit a spherical shape (e.g., Miyahara et al. 2011; Piet et al. 2016). Instead, they have either a subhedral-euhedral shape (faceted morphology) or an anhedral shape, which probably depends on whether ferropericlase occurs as a liquidus phase or an interstitial phase, respectively. Second, immiscible melts are products of chemical segregation of an originally homogeneous melt due to changes of physicochemical conditions. During the segregation process, immiscible mafic melts are expected to have

different Mg# values (e.g., Zhang and Hsu 2009; Zhang et al. 2012). However, this is of conflict with the observation in this study that the (Mg,Fe)-oxides and surrounding silicate melt have comparable Mg# values. Thus, the spherical shape of (Mg,Fe)-oxides is not a product of immiscible melts.

A spherical shape and a protrusion surface are not unusual for minerals crystallized with either a monomer-by-monomer growth model or a polymer-by-polymer growth model (Kirkpatrick 1975; Rodríguez-González et al. 2013; De Yoreo et al. 2015). However, for minerals that crystallized from melts, their external morphologies are dependent on their latent heats of fusion, as reviewed by Kirkpatrick (1975). Materials with small latent heats of fusion should have rough interfaces and grow with a nonfaceted morphology, while those with large latent heats should have smooth interfaces and grow with a faceted morphology (Kirkpatrick 1975). Therefore, for minerals that crystallized as a liquidus phase from high-pressure and high-temperature melts, they should have either rough interfaces with a nonfaceted morphology or smooth interfaces with a faceted morphology. Given the distinction in interfaces and external morphologies of ferropericlase in Piet et al. (2016) and this study, it is very likely that the spherical ferropericlase grains with a protrusion surface in this study have crystallized with a nucleation and growth mechanism different from that for euhedral ferropericlase grains.

The presence of magnesioferrite intergrowth with ferropericlase cannot be readily interpreted with a monomer-by-monomer nucleation and growth model. Based on the latest phase relations of $MgFe_2O_4$ (Uenver-Thiele et al. 2017), magnesioferrite is stable up to approximately 9−10 GPa. It is not expected to be present under the high-temperature and high-pressure (HT-HP) conditions when ferropericlase crystallized (~24 GPa and

~1800−2000 °C, Wang et al. 2017). If the magnesioferrite had directly crystallized from the high-pressure and high-temperature silicate melt, postdating the formation of ferropericlase, it would be in direct contact with the silicate glass and relatively lower-pressure silicate minerals might also be present. However, this is conflict with the observation (Fig. 7), although magnesioferrite mainly occurs adjacent to the interface between ferropericlase and surrounding silicate glass. Therefore, the magnesioferrite should be of secondary origin and a nucleation and growth model other than monomer-by-monomer addition should be proposed to interpret the development of the spherical intergrowth of magnesioferrite and ferropericlase with a protrusion surface. Here, we suggest that crystallization by particle attachment in HT-HP silicate melts may explain all of the features of the ferropericlase-magnesioferrite intergrowth.

Although not being definitive indicators of crystallization by particle attachment, external morphology is an important clue of particle attachment growth (De Yoreo et al. 2015). The spherical shape and the protrusion surface of (Mg,Fe)-oxides can be well explained with particle attachment within a silicate melt (c.f., De Yoreo et al. 2015 and references therein). The small particles attached with each other and formed spherical clusters with a protrusion surface. The microtexture with mottle domains could be related to the presence of local lattice strain (Langenhorst et al. 2011; Hu and Sharp 2017), if it is not totally due to ion-beam damage during FIB sample preparation. If this is correct, the size of different domains probably reflects the size distribution of the primary particles prior to particle attachment. Besides the potential evidence from external morphology and microtexture, thermodynamic and kinetic factors will be considered to qualitatively explain the crystallization by particle attachment (De Yoreo et al. 2015). First, a free-energy

landscape that determines the thermodynamic preference for particle structure, shape, and size distribution should be present during crystallization by particle attachment. When the cooling curve crosses the landscape, particle attachment may take place (De Yoreo et al. 2015). Second, dynamic processes, such as particle diffusion and relaxation, determine whether the growth process follows this preference or not (De Yoreo et al. 2015).

As stated above, magnesioferrite in the spherical grains of (Mg,Fe)-oxides should be a secondary phase. This implies the presence of a transitional precursor phase for the ferropericlase-magnesioferrite intergrowth (Uenver-Thiele et al. 2017). We propose that the transitional phase is non-stoichiometric ferropericlase that contains both ferric ions and cation vacancy corresponding to the magnesioferrite stoichiometry. With the presence of cation vacancy, the non-stoichiometric ferropericlase would have a slightly higher free energy and is a metastable phase under high-pressure and high-temperature conditions, compared to the stable phases (vacancy-free ferropericlase and magnesioferrite). Therefore, the presence of transitional Fe^{3+}, vacancy-bearing ferropericlase meets the requirement for the presence of a free-energy landscape (De Yoreo et al. 2015). The presence of such a transitional Fe^{3+}, vacancy-bearing ferropericlase could be related to rapid cooling, which is supported by the almost identical Mg# values between the ferropericlase-magnesioferrite intergrowth and surrounding silicate glass. Previous investigations found large Mg-Fe differentiation between equilibrated ferropericlase and silicate phases (e.g., Miyahara et al. 2011; Nakajima et al. 2012; Piet et al. 2016). If the ferropericlase-magnesioferrite intergrowth is chemically equilibrated with surrounding silicate glass, the (Mg,Fe)-oxides intergrowth would be highly enriched in Fe compared to surrounding silicate glass (Miyahara et al. 2011). However, this is not observed in this study. The fact that no low-

297 pressure silicate minerals crystallized in the silicate glass also supports that the shocked
298 melt pocket has quenched very rapidly.

299 The transitional Fe^{3+}, vacancy-bearing ferropericlase could have a crystal structure
300 similar to ferropericlase with a high crystallographic (isometric) symmetry. The high
301 crystallographic symmetry increases the probability that the transitional particles attach
302 with surrounding particles and do not detach again, since the crystals with high symmetry
303 can readily find lattice-matched crystal faces to form relatively strong chemical bonds. At
304 the early stage of crystallization, the transitional particles are small (probably 2–10 nm in
305 size), and particle attachment would enhance the sizes of aggregates and their stability in
306 high-temperature melts. Therefore, the presence of a transitional, Fe^{3+}, vacancy-bearing
307 ferropericlase meets the thermodynamic requirement for crystallization by particle
308 attachment.

309 Although no simulation experiment about the particle migration speed of
310 ferropericlase in silicate melt under HT-HP conditions has been reported, the layered
311 distribution of the oxide spherules in silicate melt (Fig. 1b) strongly indicates particle
312 migration of the (Mg,Fe)-oxides grains with a distance of 1−2 μm. In theory, the Brownian
313 motion of transitional Fe^{3+}, vacancy-bearing ferropericlase in the silicate melt should have
314 been enhanced by high temperatures and increases the probability of particle attachment
315 (Huang et al. 2003; Penn 2004). High-temperature mafic melts contain relatively low
316 abundance of net-forming cations and would have a low viscosity, which is favorable for
317 the Brownian motion of particles. This would account for the possibility of particle
318 attachment during the short high-pressure and high-temperature intervals. Columbic
319 interaction, van der Waals attraction, and random Brownian force have been proposed as

the driving forces for particle attachment in previous investigations (Gibbs et al. 2011; Zhang and Banfield 2012; Raju et al. 2014; Zhang et al. 2014; Chen et al. 2015; Zhang et al. 2017). Some, if not all, of them probably play an important role as a driving force of particle attachment. In addition, Fe^{3+}-bearing wüstite is magnetic (Gheisari et al. 2008). Therefore, it is also likely that magnetic attraction among the transitional Fe^{3+}-bearing ferropericlase grains is another driving force for particle attachment.

After the particle attachment, when the pressure and temperature decrease, the small Fe^{3+}, vacancy-bearing ferropericlase was unstable and vacancy-free-ferropericlase and magnesioferrite become stable instead. This process could be companied with Ostwald Ripening (Penn 2004; De Yoreo et al. 2015). During this process, ferric ions and cation vacancy would diffuse in ferropericlase. The consequence is the formation of magnesioferrite adjacent to the interface between the oxides intergrowth and surrounding silicate glass and the elimination of cation vacancy. This structural rearrangement could be very fast if we mainly consider the motion of cation vacancy in ferropericlase. Using the diffusion coefficient reported in reference (Sempolinsky and Kingery 1980) and the upper limit of temperature of the stability field for magnesioferrite (1600 ^{o}C, Uenver-Thiele et al. 2017), it takes only 36 ns for an average diffusion distance of 100 nm. This time-scale is very short, even compared to the duration for solidification of the melts with a net thickness of several micrometers (hundreds of nanoseconds to tens of microseconds; Langenhorst and Poirier 2000). Therefore, kinetically, the formation of the ferropericlase-magnesioferrite intergrowth can also be well explained by crystallization via particle attachment.

342 Comparing crystallization by particle attachment in aqueous solutions (De Yoreo et
343 al. 2015), high-temperature silicate melts (this study), and supersaturated vapor (Ishizuka
344 et al. 2016), they probably share at least two similarities. The first similarity is their
345 formation mechanisms. In aqueous solutions, crystallization by particle attachment always
346 involves metastable particles or phases no matter what the pathway is (De Yoreo et al.
347 2015). In high-temperature melts and vapors, a transitional phase with a higher free energy
348 is also involved (this study and Ishizuka et al. 2016). It seems that the presence of
349 metastable particles or phases is one of the common factors for crystallization by particle
350 attachment in various systems. The second similarity could be enough numbers and free
351 motions of the metastable particles that enables efficient particle attachment.

352 Except for these similarities, there are a few differences for crystallization by particle
353 attachment among various systems. The first is apparently temperature. Most cases that
354 have been reported are under low-temperature aqueous solution conditions (see De Yoreo
355 et al. 2015). Motion of particles or phases in aqueous solutions and high-temperature
356 vapors could be very fast. However, at low temperatures, the motion of particles and phases
357 in the silicate melts would be very slow due to its higher viscosity and the attachment
358 efficiency will be very low. Therefore, high temperature is very critical for the presence of
359 particle attachments in silicate melts. Second, the interaction forces between the
360 transitional phase and surrounding materials are largely different in various systems. For
361 aqueous solutions, the interaction between hydroxyl and the metastable particles is an
362 important force. However, this interaction force would not so important in high-
363 temperature vapors and anhydrous melts. For high-temperature low-pressure vapors
364 (Ishizuka et al. 2016), molecules probably have weak interaction. Brownian motion could

be the major driving force of particle attachment. In contrast, for anhydrous silicate melts, Al^{3+} and Si^{4+} would form well-polymerized silicate networks, which probably suppress the motion of metastable particles. However, the presence of abundant net-modifying cations such as Mg^{2+} and Fe^{2+} in ultramafic to mafic melts (the case in this study) reduce its viscosity (e.g., Giordano et al. 2008). The effect could enhance particle attachment in the melts. Since potential crystallization by particle attachment in high-temperature systems has only been realized recently (this study and Ishizuka et al. 2016), more investigations are needed to decipher the similarities and differences among different systems.

IMPLICATIONS

The formation of ferropericlase-magnesioferrite intergrowth in this study can be best explained with crystallization by particle attachment, which is probably followed by Ostwald Ripening. A schematic diagram of this process is shown in Fig. 9. The (Mg,Fe)-oxides intergrowth had a transitional, non-stoichiometric ferropericlase that contains both ferric ions and cation vacancy. Under HT-HP conditions, the transitional non-stoichiometric ferropericlase particles with a high crystallographic symmetry aggregated with each other probably by random Brownian force, or/and van der Waals attraction or/and magnetic attraction and larger spherical and oval-like aggregates formed with surface protrusion and internal microtexture. Subsequent to the particle attachment, the (Mg,Fe)-oxides experienced a process of Ostwald Ripening. Small particles dissolved and large grains formed. Meanwhile, ferric ions and cation vacancy diffused in ferropericlase and then magnesioferrite formed adjacent to the boundaries between ferropericlase and surrounding silicate glass.

Differing the comparatively low-temperature aqueous systems with crystallization by particle attachment in previous investigations, the crystallization of (Mg,Fe)-oxides by particle attachment described in this study took place in high-temperature melts. This has significant implications for understanding the early-stage, especially nucleation and growth of crystalline phases with a relatively high crystallographic symmetry in high temperature melts far from equilibrium. Combining with the work by Ishizuka et al. (2016), the potential, high-temperature systems may contain, but not limited to, exploding stars, chondrules in the solar nebula, erupted volcanic melts, and even intruded magmas. At the early stages of these high-temperature systems, transitional nanocrystalline phases with a high crystallographic symmetry (e.g., metal, sulfide, and oxide) may nucleate and aggregate with each other and form larger grains in subsequent Ostwald Ripening processes. Due to the presence of metastable phases, the materials that have crystallized by particle attachment probably have isotopic fractionation behaviors different from those formed by monomer-by-monomer addition, which is deserved to be studied by future synthetic experiments and theoretical calculations.

ACKNOWLEDGEMENTS

This work was financially supported by Natural Science Foundations of China (grant 41673068) and Jiangsu Province of China (grant BK20170017). We thank two anonymous reviewers for their helpful comments and Associate Editor E. Bruce Watson for his editorial efforts.

REFERENCES CITED

Banfield, J.F., Welch, S.A., Zhang, H.Z., Ebert, T.T., and Penn, R.L. (2000) Aggregation-based crystal growth and microstructure development in natural iron oxyhydroxide biomineralization products. Science, 289, 751−754.

Chen, Q., Cho, H., Manthiram, K., Yoshida, M., Ye, X., and Alivisatos, A.P. (2015) Interaction potentials of anisotropic nanocrystals from the trajectory sampling of particle motion using in situ liquid phase transmission electron microscopy. ACS Central Science, 1, 33−39.

De Yoreo, J.J., Gilbert, P.U.P.A., Sommerdijk, N.A.J.M., Penn, R.L., Whitelam, S., Joester, D., Zhang, H., Rimer, J.D., Navrotsky, A., Banfield, J.F., Wallace, A.F., Michel, F.M., Meldrum, F.C., Cölfen, H., and Dove, P.M. (2015) Crystallization by particle attachment in synthetic, biogenic, and geologic environments. Science, 349, aaa6760. DOI: 10.1126/science.aaa6760.

Gheisari, M., Mozaffari, M., Acet, M., and Amighian, J. (2008) Preparation and investigation of magnetic properties of wüstite nanoparticles. Journal of Magnetism and Magnetic Materials, 320, 2618−2621.

Gibbs, G.V., Crawford, T.D., Wallace, A.F., Cox, D.F., Parrish, R.M., Hohenstein, E.G., and Sherrill, C.D. (2011) Role of long-range intermolecular forces in the formation of inorganic nanoparticle clusters. The Journal of Physical Chemistry A, 115, 12933−12940.

Giordano, D., Russell, J.K., and Dingwell, D.B. (2008) Viscosity of magmatic liquids: A model. Earth and Planetary Science Letters, 271, 123–134.

Hallis, L.J., Huss, G.R., Nagashima, K., Taylor, G.J., Stöffler, D., Smith, C.L., and Lee, M.R. (2017) Effects of shock and Martian alteration on Tissint hydrogen isotope ratios and water content. Geochimica et Cosmochimica Acta, 200, 280−294.

Hu, J.P., and Sharp, T.G. (2017) Back-transformation of high-pressure minerals in shocked chondrites: Low-pressure mineral evidence for strong shock. Geochimica et Cosmochimica Acta, 215, 277−294.

Huang, F., Zhang, H.Z., and Banfield, J.F. (2003) Two-stage crystal growth kinetics observed during hydrothermal coarsening of nanocrystalline ZnS. Nano Letters, 3, 373−378.

Ishizuka, S., Kimura, Y., Yamazaki, T., Hama, T., Watanabe, N., and Kouchi, A. (2016) Two-step process in homogeneous nucleation of alumina in supersaturated vapor. Chemistry of Materials, 28, 8732−8741.

Ivanov, V.K., Fedorov, P.P., Baranchikov, A.Y., and Osiko, V.V. (2014) Oriented attachment of particles: 100 years of investigations of non-classical crystal growth. Russian Chemical Reviews, 83, 1204−1222.

Kirkpatrick, R.J. (1975) Crystal growth from the melt: a review. American Mineralogist, 60, 798−814.

Langenhorst, F., and Poirier, J.P. (2000) Anatomy of black veins in Zagami: clues to the formation of high-pressure phases. Earth and Planetary Science Letters, 184, 37−55.

Langenhorst, F., Harries, D., and Pollok, K. (2011) Non-stoichiometry, defects and superstructures in sulfide and oxide minerals. In: Nieto, F., and Livi, K.J.T. (Eds.), Minerals at the Nanoscale. European Mineralogical Union Notes in Mineralogy, 14, 261−295.

Miyahara, M., Ohtani, E., Ozawa, S., Kimura, M., El Goresy, A., Sakai, T., Nagase, T., Hiraga, K., Hirao, N., and Ohishi, Y. (2011) Natural dissociation of olivine to (Mg,Fe)SiO_3 perovskite and magnesiowüstite in a shocked Martian meteorite. Proceedings of Natural Academy of Sciences of the United States of America, 108, 5999−6003.

Nakajima, Y., Frost, D.J., and Rubie, D.C. (2012) Ferrous iron partitioning between magnesium silicate perovskite and ferropericlase and the composition of perovskite in the Earth's lower mantle. Journal of Geophysical Research, 117, B08201.

Pang, R.L., Harries, D., Pollok, K., Zhang, A.C., and Langenhorst, F. (2018) Vestaite, $(Ti^{4+}Fe^{2+})Ti^{4+}{}_3O_9$, a new mineral in the shocked eucrite Northwest Africa 8003. American Mineralogist, 103, 1502−1511.

Pang, R.L., Zhang, A.C., Wang, S.Z., Wang, R.C., and Yurimoto, H. (2016) High-pressure minerals in eucrite suggest a small source crater on Vesta. Scientific Reports, 6, 26063.

Penn, R.L. (2004) Kinetics of oriented aggregation. Journal of Physical Chemistry B, 108, 12707−12712.

Penn, R.L., and Banfield, J.F. (1998) Imperfect oriented attachment: dislocation generation in defect-free nanocrystals. Science, 281, 969−971.

Piet, H., Badro, J., Nabiei, F., Dennenwaldt, T., Shim, S., Cantoni, M., Hébert, C., and Gillet, P. (2016) Spin and valence dependence of iron partitioning in Earth's deep mantle. Proceeding of the National Academy of Sciences of the United States of America, 113, 11127−11130.

Raju, M., van Duin, A.C.T., and Fichthorn, K.A. (2014) Mechanisms of oriented attachment of TiO_2 nanocrystals in vacuum and humid environments: reactive molecular dynamics. Nano Letters, 14, 1836−1842.

Rodríguez-González, B., Vereda, F., de Vicente, J., Hidalgo-Álvarez, R. (2013) Rough and hollow spherical magnetite microparticles: revealing the morphology, internal structure, and growth mechanism. The Journal of Physical Chemistry, 117, 5397−5406.

Sempolinsky, D.R., and Kingery, W.D. (1980) Ionic conductivity and magnesium vacancy mobility in magnesium oxide. Journal of the American Ceramic Society, 63, 664−669.

Sharp, T.G., and DeCarli, P.S. (2006) Shock effects in meteorites. In: Lauretta, D.S., and McSween, H.Y. (Eds.), Meteorites and the Early Solar System II. The University of Arizona Press, pp. 653–677.

Uenver-Thiele, L., Woodland, A.B., Boffa Ballaran, T., Miyajima, N., and Frost, D.J. (2017) Phase relations of $MgFe_2O_4$ at conditions of the deep upper mantle and transition zone. American Mineralogist, 102, 632−642.

Van Aken, P.A., and Liebscher, B. (2002) Quantification of ferrous/ferric ratios in minerals: new evaluation schemes of Fe L_{23} electron energy-loss near-edge spectra. Physics and Chemistry of Minerals, 29, 188−200.

Wang, S.Z., Zhang, A.C., Pang, R.L., Chen, J.N., Gu, L.X., and Wang, R.C. (2017) Petrogenesis and shock metamorphism of the enriched lherzolitic shergottite Northwest Africa 7755. Meteoritics & Planetary Science, 52, 2437−2457.

494 Zhang, A.C. and Hsu, W.B. (2009) Petrography, mineralogy, and trace element
495 geochemistry of lunar meteorite Dhofar 1180. Meteoritics & Planetary Science, 44,
496 1265−1286.
497 Zhang, A.C., Taylor, L.A., Wang, R.C., Li, Q.L., Li, X.H., Patchen, A.D., and Liu Y. (2012)
498 Thermal history of Apollo 12 granite and KREEP-rich rock: Clues from Pb/Pb ages
499 of zircon in lunar breccia 12013. Geochimica et Cosmochimica Acta, 95, 1−14.
500 Zhang, H.Z., and Banfield, J.F. (2012) Energy calculations predict nanoparticle attachment
501 orientations and asymmetric crystal formation. The Journal of Physical Chemistry
502 Letters, 3, 2882−2886.
503 Zhang, H.Z., De Yoreo, J.J., and Banfield, J.F. (2014) A unified description of attachment
504 based crystal growth. ACS Nano, 8, 6526−6530.
505 Zhang, X., He, Y., Sushko, M.L., Liu, J., Luo, L., De Yoreo, J.J., Mao, S.X., Wang, C.,
506 and Rosso, K.M. (2017) Direction-specific van der Waals attraction between rutile
507 TiO_2 nanocrystals. Science, 356, 434−437.
508

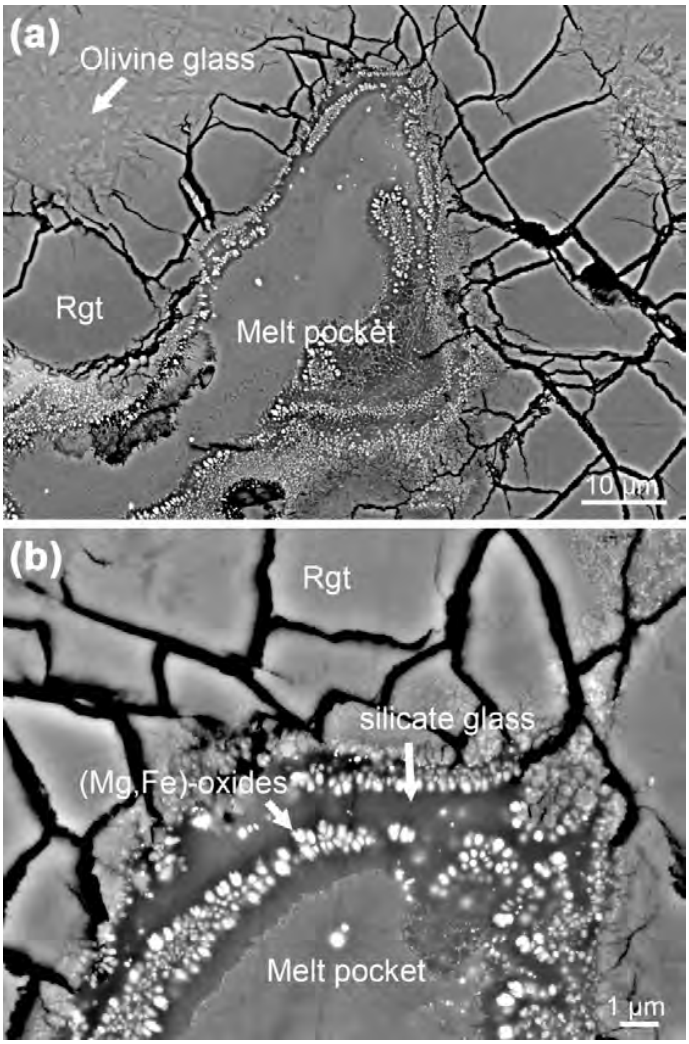

Figure 1. Shock-induced melt pocket in NWA 7755. The melt pocket is partly enclosed by ringwoodite. In the melt pocket, spherical and oval-shaped (Mg,Fe)-oxides occurs in silicate glass and form aggregates parallel to the boundary between ringwoodite and melt pocket.

This is a preprint, the final version is subject to change, of the American Mineralogist (MSA)
Cite as Authors (Year) Title. American Mineralogist, in press.
DOI: https://doi.org/10.2138/am-2019-6597

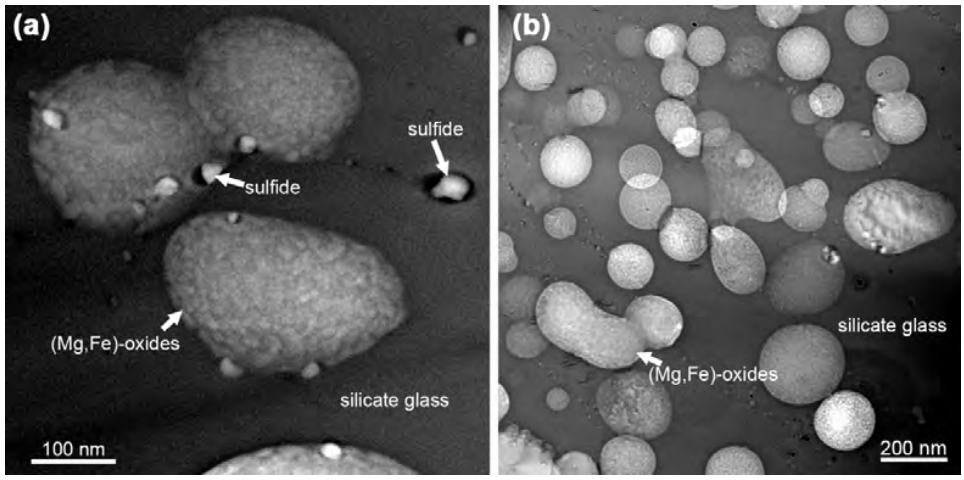

Figure 2. HAADF-STEM images of spherical grains of (Mg,Fe)-oxides in NWA 7755. (a-b) The spherical grains of (Mg,Fe)-oxides are surrounded by silicate glass. All of these spherical grains of (Mg,Fe)-oxides have surface protrusions.

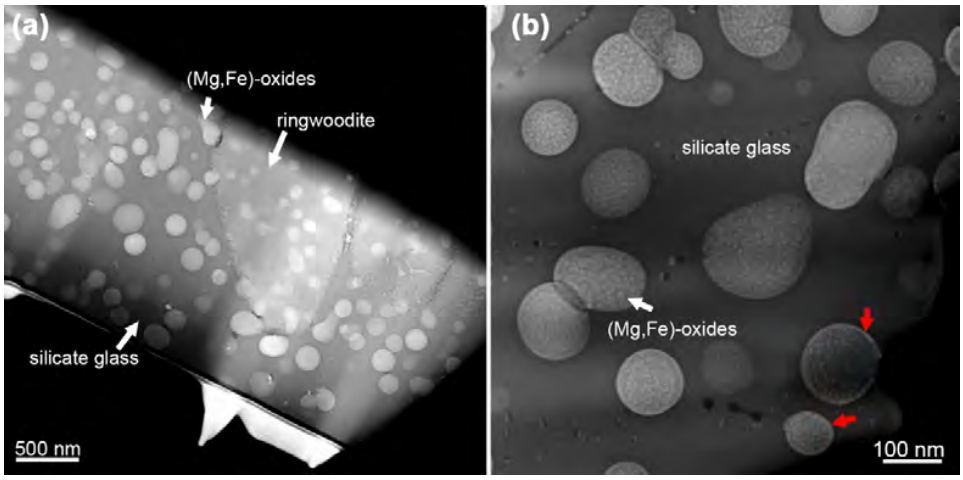

Figure 3. HAADF-STEM images of the TEM foils showing the occurrence of (Mg,Fe)-oxides spherules in silicate glass. All of the (Mg,Fe)-oxides spherules show surface protrusion. In (a), relict ringwoodite grains are present with curved outlines. Note the bright rims of (Mg,Fe)-oxides spherules indicated with red arrows in (b).

This is a preprint, the final version is subject to change, of the American Mineralogist (MSA)
Cite as Authors (Year) Title. American Mineralogist, in press.
DOI: https://doi.org/10.2138/am-2019-6597

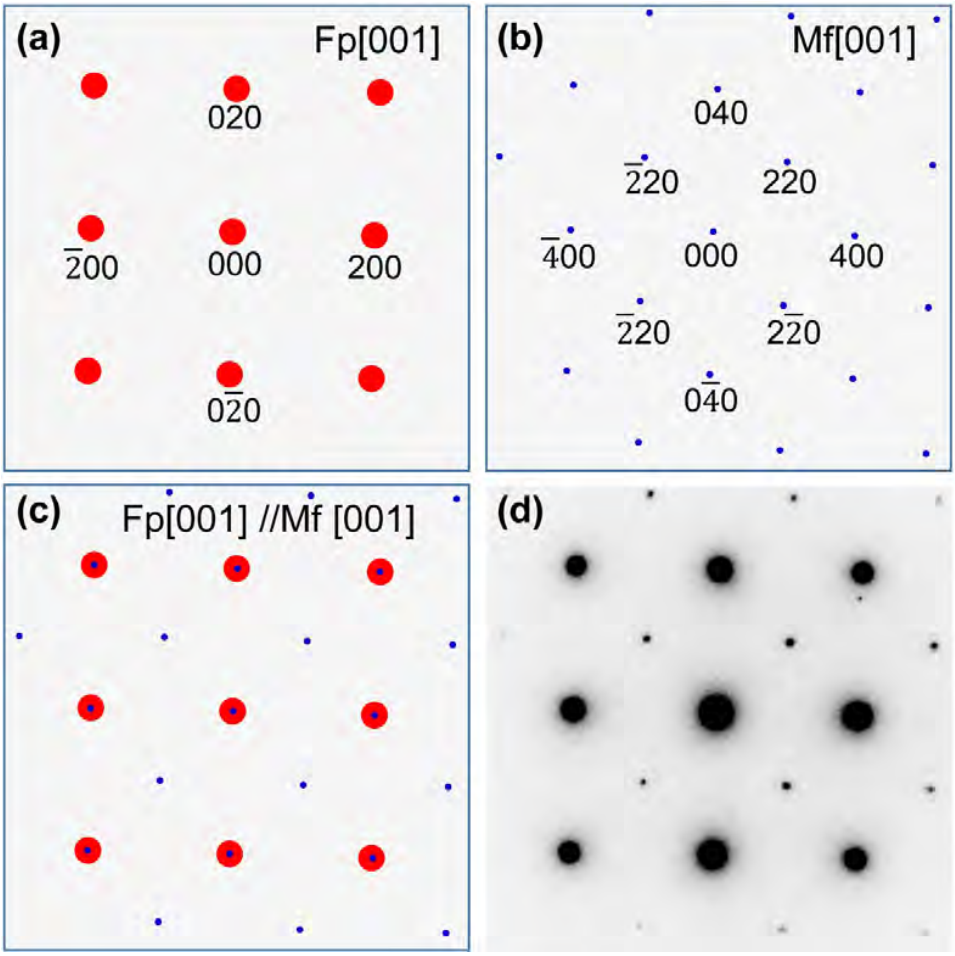

Figure 4. Schematic and observed selected area electron diffraction (SAED) patterns of (Mg,Fe)-oxides. (a-b) Schematic SAED patterns of ferropericlase (Fp) and magnesioferrite (Mf) along [001] zone axis. (c) Schematic SAED pattern of ferropericlase and magnesioferrite with Fp[001] //Mf[001]. (d) The SAED pattern of the ferropericlase and magnesioferrite intergrowth in NWA 7755.

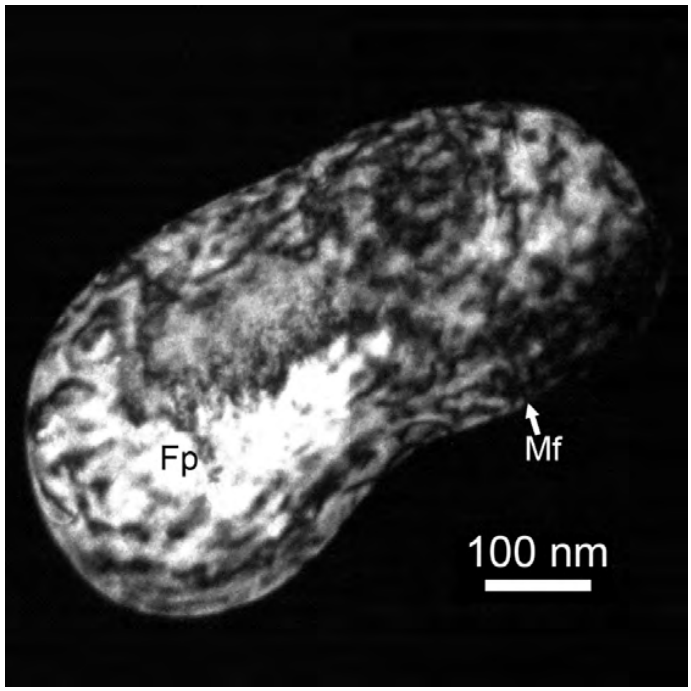

530

531 Figure 5. Dark-field image of (Mg,Fe)-oxides in NWA 7755. The 111 diffraction spot of
532 magnesioferrite was used for the dark-field image. The bright phase is ferropericlase (Fp)
533 and the dark phase is magnesioferrite (Mf).

This is a preprint, the final version is subject to change, of the American Mineralogist (MSA)
Cite as Authors (Year) Title. American Mineralogist, in press.
DOI: https://doi.org/10.2138/am-2019-6597

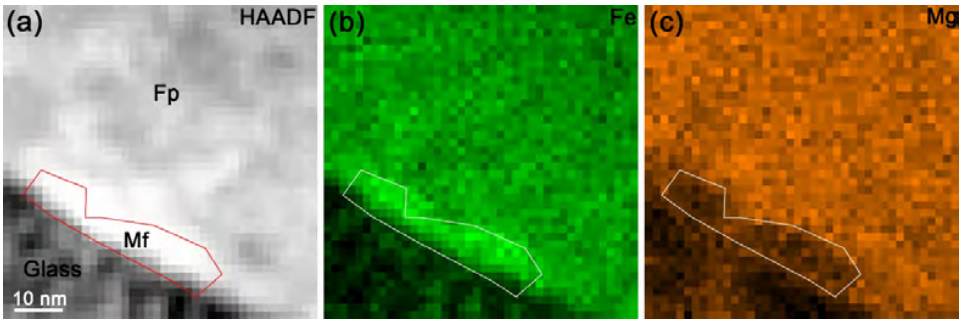

Figure 6. TEM-EDS mapping results of the intergrowth of ferropericlase and magnesioferrite. The magnesioferrite (Mf) occurs adjacent to the boundary between ferropericlase (Fp) and surrounding glass. The magnesioferrite contains higher Fe and less Mg than the ferropericlase. The magnesioferrite region was outlined based on the enrichment of Fe and depletion of Mg.

This is a preprint, the final version is subject to change, of the American Mineralogist (MSA)
Cite as Authors (Year) Title. American Mineralogist, in press.
DOI: https://doi.org/10.2138/am-2019-6597

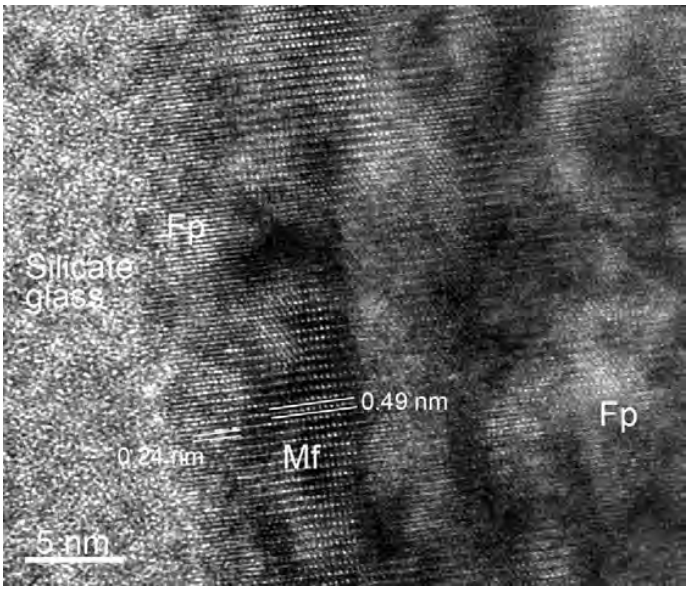

Figure 7. High-resolution TEM image of the intergrowth of ferropericlase (Fp) and magnesioferrite (Mf). The magnesioferrite is present adjacent to the boundary between ferropericlase and silicate glass. The magnesioferrite illustrates continuity of lattice fringes with ferropericlase. The ferropericlase region shows a mottled microtexture.

This is a preprint, the final version is subject to change, of the American Mineralogist (MSA)
Cite as Authors (Year) Title. American Mineralogist, in press.
DOI: https://doi.org/10.2138/am-2019-6597

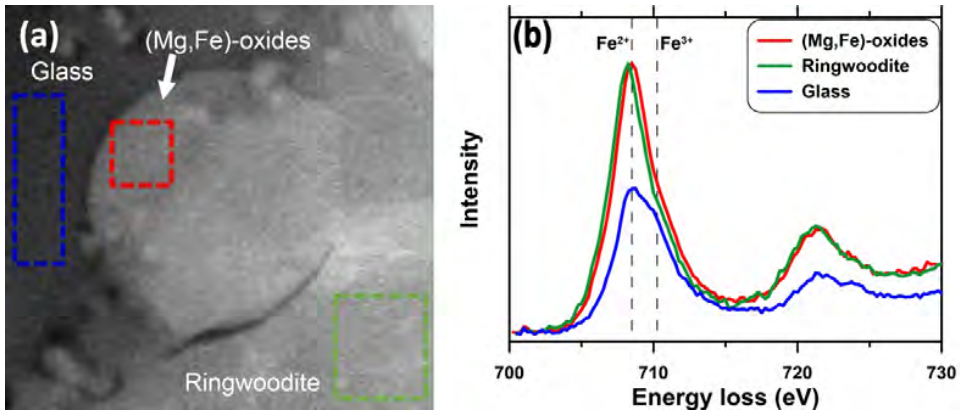

Figure 8. HAADF image and EELS spectra of (Mg,Fe)-oxides, ringwoodite (Rgt), and silicate glass. The three colored rectangles indicate the areas where EELS spectra were integrated to obtain the spectra shown in (b).

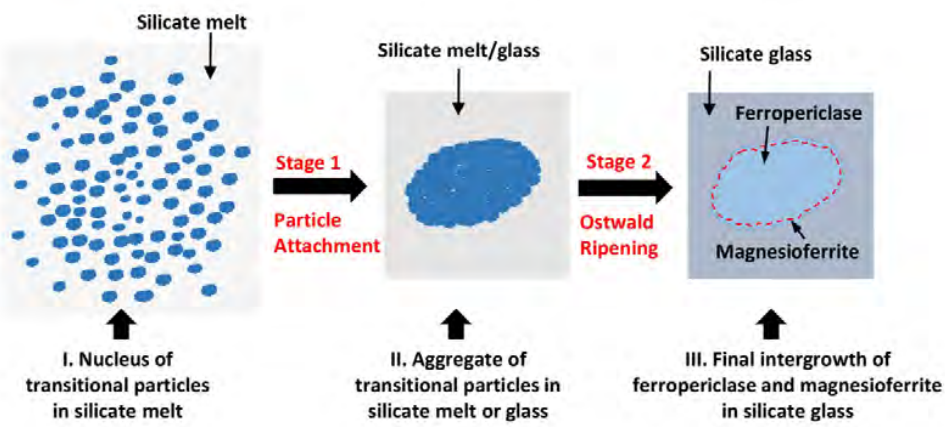

549

550 Figure 9. Cartoon diagram of crystallization of spherical intergrowth of ferropericlase and
551 magnesioferrite by particle attachment.

This is a preprint, the final version is subject to change, of the American Mineralogist (MSA)
Cite as Authors (Year) Title. American Mineralogist, in press.
DOI: https://doi.org/10.2138/am-2019-6597

552 Supplementary Table 1. TEM-EDS data for (Mg,Fe)-oxides

	1	2	3	4	5	6	7	8	9	10
MgO	50.23	52.93	51.76	47.45	43.69	45.51	48.80	51.55	54.61	51.02
FeO	49.77	47.07	48.24	52.55	56.31	54.49	51.20	48.45	45.39	48.98
Total	100	100	100	100	100	100	100	100	100	100
	Calculated on the basis of 2 oxygen atoms									
Mg	1.290	1.339	1.318	1.238	1.165	1.201	1.263	1.314	1.368	1.304
Fe	0.710	0.661	0.682	0.762	0.835	0.799	0.737	0.686	0.632	0.696
Mg#	0.64	0.67	0.66	0.62	0.58	0.60	0.63	0.66	0.68	0.65

553

This is a preprint, the final version is subject to change, of the American Mineralogist (MSA)
Cite as Authors (Year) Title. American Mineralogist, in press.
DOI: https://doi.org/10.2138/am-2019-6597

554 Supplementary Table 2. TEM-EDS data for silicate glass associated with (Mg,Fe)-
555 oxides

	1	2	3	4	5	6	7
MgO	23.22	22.59	22.02	24.61	24.24	24.41	24.50
Al_2O_3	1.46	1.41	1.63	1.67	1.53	1.41	1.40
SiO_2	45.21	45.12	44.28	46.48	46.60	46.54	45.15
P_2O_5	0.83	0.94	1.13	0.84	1.15	1.06	1.15
CaO	3.11	3.12	3.31	2.93	3.55	3.35	3.47
TiO_2	0.82	0.85	0.94	0.75	0.91	0.98	1.07
MnO	0.62	0.59	0.51	0.47	0.54	0.43	0.49
FeO	24.73	25.39	26.18	22.25	21.47	21.82	22.79
Total	100	100	100	100	100	100	100
	Calculated on the basis of 4 oxygen atoms						
Mg	0.897	0.875	0.858	0.936	0.919	0.927	0.938
Al	0.044	0.043	0.050	0.050	0.046	0.042	0.042
Si	1.165	1.165	1.150	1.178	1.178	1.178	1.153
P	0.018	0.021	0.025	0.018	0.024	0.023	0.025
Ca	0.086	0.086	0.092	0.079	0.096	0.091	0.095
Ti	0.016	0.016	0.018	0.014	0.017	0.019	0.020
Mn	0.014	0.013	0.011	0.010	0.012	0.009	0.011
Fe	0.531	0.546	0.566	0.470	0.452	0.460	0.485
Cations	2.770	2.766	2.770	2.756	2.745	2.748	2.768
Mg#	0.63	0.62	0.60	0.67	0.67	0.67	0.66
(Mg+Fe+Ca)/Si	1.30	1.29	1.32	1.26	1.25	1.25	1.32

556